Plasmonics (2022) 17:1831–1841
https://doi.org/10.1007/s11468-022-01669-w

# Design of High-Sensitivity Surface Plasmon Resonance Sensor Based on Nanostructured Thin Films for Effective Detection of DNA Hybridization

**Reza Ghayoor[1] · Soraya Zangenehzadeh[2] · Alireza Keshavarz[2]**

Received: 24 February 2022 / Accepted: 31 May 2022 / Published online: 15 June 2022


**Abstract**
As developed countries' ability to control infectious diseases increases, it has become clear that genetic diseases are a major cause of disability, death, and human tragedy. Coronavirus has recently spread throughout the world, and the capacity to detect low concentrations and virus changes can help to prevent the sickness from spreading further. In this paper, a surface plasmon resonance sensor based on nanostructured thin films and graphene as a 2D material has been designed with high sensitivity and accuracy to identify DNA-based infectious diseases such as SARS-CoV-2. The transfer matrix method assesses the effects of different structural factors, including nanolayer thickness on the sensor's performance. The results demonstrated that the sensor with the Kretschmann configuration has ultra-high sensitivity (192.19 deg/RIU) and a high figure of merit (634.68 $RIU^{-1}$).

**Keywords** Biosensor based on the thin film · Coronavirus · Quasi-photonic crystal · Graphene · Surface plasmon resonance

## Introduction

The sensors based on arrays of immobilized single-stranded DNA (ss-DNA) are known as quick, sensitive, and stable methods for the detection of sequencing of the human genome and the diagnosis of genetic disease. The performance of these sensors is based on the hybridization of active sites of ss-DNA molecules (probe) with the liquid sample containing the DNA target. Hybridization detection can be obtained through electrochemical or optical properties changes due to nonspecifically adsorbed target molecules. The physical absorption of DNA target molecules can be monitored with the surface plasmon resonance (SPR) method [1–4].

The SPR is related to the quantum of massive oscillations of free electrons in a metal–dielectric interface. The presence of a surface or interface between materials with different dielectric constants can lead to specific surface excitations, and these waves are enclosed near the interface [5–7]. Plasmon excitation necessitates a suitable structural layout, which can be accomplished via techniques such as the attenuated total reflection (ATR) configuration. ATR uses infrared (IR) spectroscopy as a transmission method for chemical or biological processes. In contrast to transmission techniques, which require light to pass through the sample, IR ATR does not require a sample thickness (liquid or solid samples can be 10 microns thick or 10 cm thick) [8]. One of the practical uses of this approach is the detection of breast cancer in saliva [9]. For sensor applications, the ATR technique can be employed in two well-known geometries: Otto and Kretschmann. The Kretschmann structure is used in the SPR sensor applications such as biochemical sensors, gas sensing, and diagnostics of medical issues. These structures include a prism, a metal, a dielectric, and a sensitive medium [10–12]. Many other plasmonic nanostructures, such as gratings, have been reported to detect changes in RI, although careful consideration of geometrical factors is required [13, 14]. The sensitivity of the SPR method can be enhanced by using alternative materials for the metal [15] and dielectric layers, as well as variations in layered topologies. Graphene is one of the 2D materials that can

✉ Alireza Keshavarz
keshavarz@sutech.ac.ir

[1] Institute for Nanoscience and Nanotechnology, Sharif University of Technology, Tehran, Iran

[2] Department of Physics, Shiraz University of Technology, Shiraz, Iran

significantly enhance localized surface plasmons due to its adjustable electrical properties [16].

Furthermore, quasi-photonic crystals as a new kind of photonic crystal have emerged [17] that are used for a variety of applications, such as waveguides [18], filters [19–21], and optical sensors [22]. Quasi-photonic crystals as the new class of stack layers give an extra degree of freedom for tailoring photonics and photonic bandgaps based on their spectral gaps in the frequency domain. The Fibonacci structure is one of the quasi-photonic crystals composed of dielectric layers [23] and is expected to improve the SPR method sensitivity.

In recent years, given the increasing need for humans to control the COVID-19 pandemic, it is necessary to use a precise tool to identify and control these respiratory infection hazards. This novel coronavirus was first discovered through viral metagenomic analyses conducted on three bronchoalveolar-lavage specimens from patients with severe pneumonia symptoms. Both coronavirus and the common cold cause respiratory disease and using the precise diagnosis method is still challenging [24, 25]. As the virus spreads worldwide, applying accurate technology to detect COVID-19 is a crucial issue. Detecting the low concentration and mutation of coronavirus in fluid body samples such as nasal mucus membrane and human blood has been tested by an available method including nasopharyngeal swabs and serologic tests. Recent studies have reported errors in COVID-19 diagnostic tests. For patients with heart problems or weakened immune systems, using non-invasive and accurate technology to test their body samples is necessary, which is possible by optical sensing [26–29].

This paper proposes a novel DNA hybridization SPR sensor based on nanostructured thin films with real-time detection. The hybridization changes in the interface between the thiol-tethered DNA film and the DNA target (i.e., the human nasopharyngeal swabs including SARS-CoV-2) were monitored with a series of SPR spectra. The introduction of the Fibonacci quasi-photonic crystal contributes to improving detection and sensitivity in the sensor.

## Design and Theoretical Model

### Proposed Structure

Quasi-photonic crystals can be grown by juxtaposing the two building blocks $H$ and $L$ where $H$ and $L$ correspond to the high and low refractive indexes materials with refractive indices $n_H$ and $n_L$, respectively. The Fibonacci sequence can be used in the quasi-photonic crystals. These structures can be produced by irregular repeating the substitution rules $H \rightarrow HL$ and $L \rightarrow HH$. The first few generations of $S_m$ in the Fibonacci sequence are as follows: $S_0 = \{H\}$, $S_1 = \{L\}$, $S_2 = \{HL\}$, $S_3 = \{LHL\}$, and $S_4 = \{HLLHL\}$ [29].

The SPR angle and the minimum reflection energy were studied for monitoring SARS-CoV-2. The configuration and the design of the proposed sensor are shown in Fig. 1. The gold metallic nanolayer (plasmonic metal) is coated on an SF10 prism, and then the Fibonacci quasi-photonic crystal is composed of graphene (as a 2D material) and $Bi_4Ti_3O_{12}$ thin films are deposited, respectively. We developed the Fibonacci quasi-photonic structure functionalized with the excellent receptor of SARS-CoV-2 as one of the applications

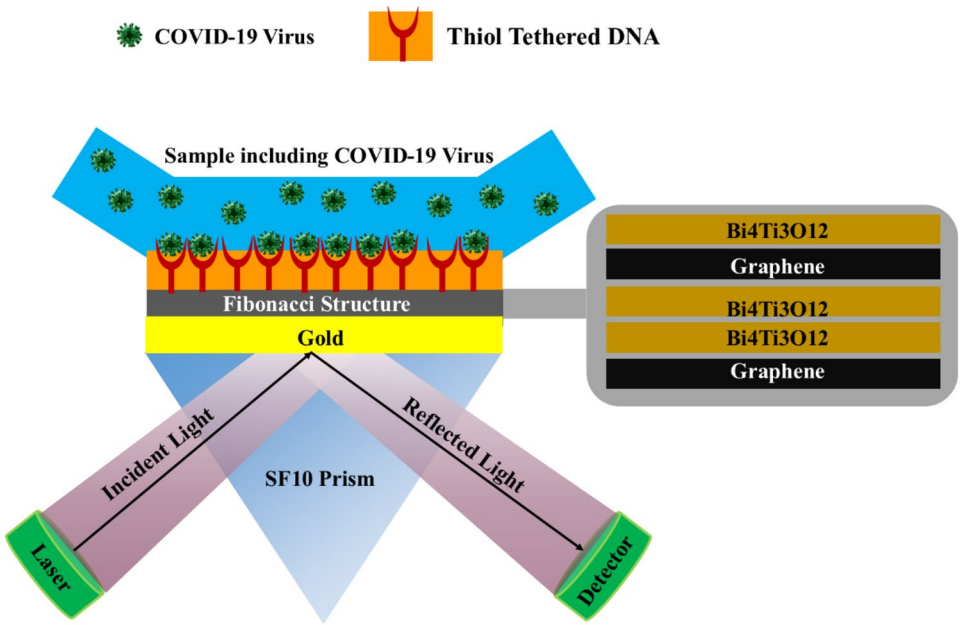


**Fig. 1** Schematic of the proposed SPR sensor configuration, including the gold nanolayer and nanostructured thin films

of the thiol-tethered DNA. Here, the antigen is the SARS-CoV-2 virus and is taken as the sensing medium in serum/nasopharyngeal swab samples.

## Computational Method

The transfer matrix method performs the reflectivity analysis in multilayer scheme sensors, which is an accurate and efficient method to calculate the reflection coefficient. This method links the magnetic and the electric fields' tangential components of the first and outer layers.

Here, the transfer matrix and Fresnel's equations investigate the incident light propagation in the sensor layers. The interface matrix will be considered as $M$ which can link the electric field of the layer $i$ to the layer $i+1$ [30]:

$$M_i = \begin{bmatrix} \cos(b_i) & -i \sin(b_i)/q_i \\ -iq_i \sin(b_i) & \cos(b_i) \end{bmatrix} \quad (1)$$

where the admittance $b_i$ and the phase shift $q_i$ parameters are defined as follows:

$$b_i = \frac{2\pi d_i}{\lambda\sqrt{n_i - (n_1 \sin\theta)^2}} \quad (2)$$

$$q_i = \frac{\sqrt{n_i - (n_1 \sin\theta)^2}}{n_i^2} \quad (3)$$

The $n_i$ and $d_i$ are the refractive index and thickness of layer $i$th, respectively, $\lambda$ is the incident light wavelength, $\theta$ is the angle of the incident light, and $n_1$ is the refractive index of the prism glass.

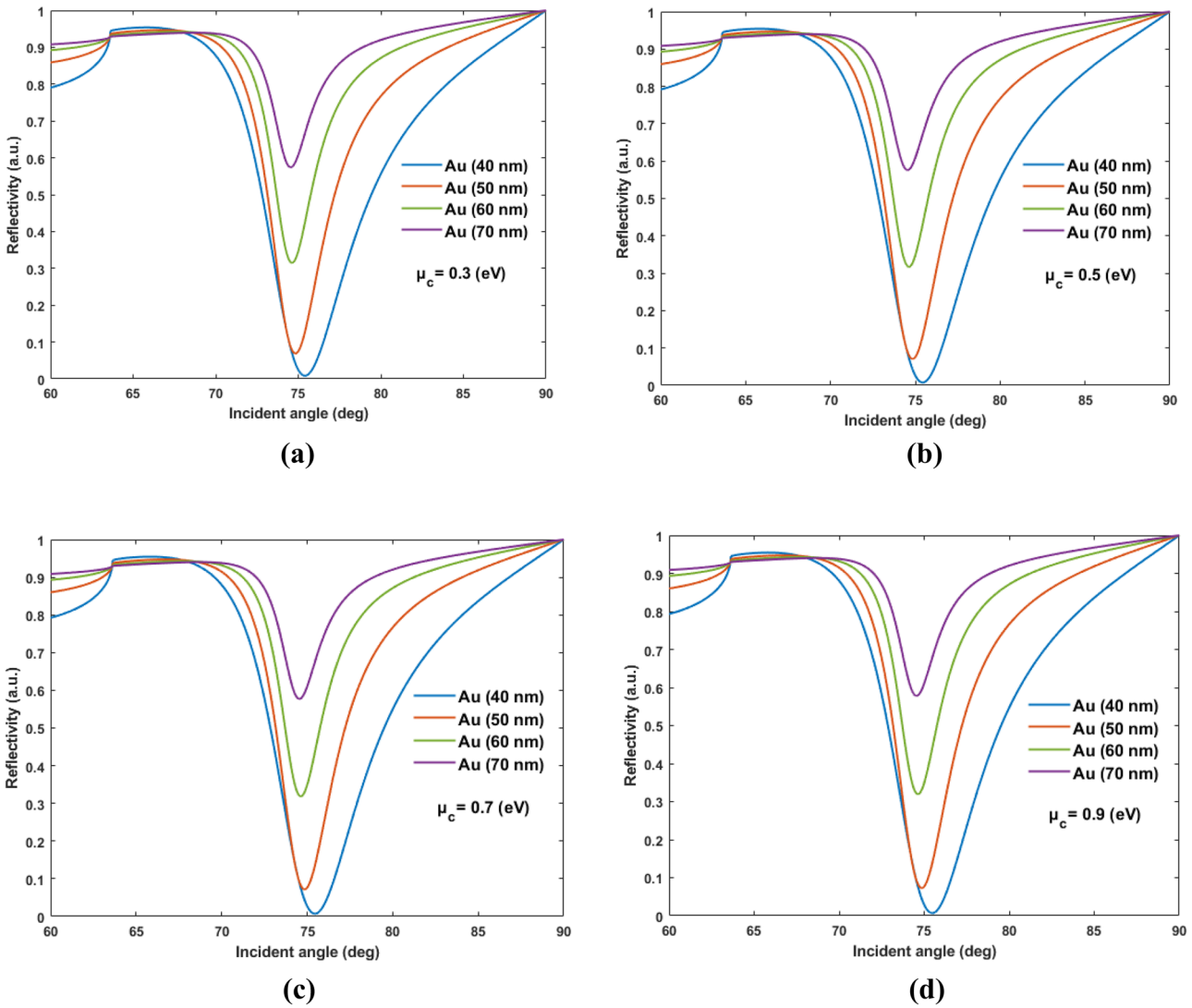


**Fig. 2** The reflectivity in SPR curve as a function of the graphene chemical potential with various thicknesses of the gold thin film **a** $\mu_c = 0.3\ eV$, **b** $\mu_c = 0.5\ eV$, **c** $\mu_c = 0.7\ eV$, and **d** $\mu_c = 0.9\ eV$; with $d_g = 4 \times 0.34\ nm$ and $d_{Bi_4Ti_3O_{12}} = 19.5\ nm$

For the sensor structure in Fig. 1, the entire matrix $U$ is obtained by the following equation:

$$U = \prod_{n=2}^{N-1} M_n \tag{4}$$

The total reflection for the p-polarized (TM) incident light wave ($r_p$) can be finally obtained from the elements of the matrix $U$ as follows [30]:

$$r_p = \frac{(U(1,1) + U(1,2)q_i)q_1 - (U(2,1) + U(2,2)q_i)}{(U(1,1) + U(1,2)q_i)q_1 + (U(2,1) + U(2,2)q_i)} \tag{5}$$

The following equation can give the reflectivity for the defined multilayer configuration:

$$R = \left| r_p \right|^2 \tag{6}$$

The principle of the SPR sensors is based on SPs interacting with the incident p-polarized light. Because the surface plasmons are not directly excited at the metallic area, the phase-matching conditions to provide the necessary momentum to excite surface plasmons are achieved by the incident of the p-polarized light on the glass prism [7].

The crucial parameters for an SPR sensor can be characterized by mainly parameters, i.e., sensitivity and figure of merit (FOM). These parameters should be high as possible for an excellent SPR-based sensor and calculated by resonance angle and reflectance curve changes in different incident angles. The sensitivity ($S$) parameter is defined as a change in the resonance angle ($\Delta\theta_{SPR}$) to a change in the refractive index of the sensing medium ($\Delta n_s$). It shows the ability of the SPR-based sensor to identify the change in the refractive index (RI) of the sensing medium and is given by [31]:

$$S = \frac{\Delta\theta_{SPR}}{\Delta n_s} \tag{7}$$

The FoM is an intelligent and essential scale that is defined as the resonance angle shift due to a change in the sensing medium divided by the FWHM:

$$FoM = \frac{\Delta\theta_{SPR}/\Delta n_s}{FWHM.R_{\min}} = \frac{S}{FWHM.R_{\min}} \tag{8}$$

where $FWHM$ is full width at half maximum of the reflectance curve.

## Results and Discussion

This configuration is stimulated by a He–Ne laser as a light excitation source with a wavelength of 632.8 nm. The refractive index of the bismuth titanate thin film in the proposed structure is considered $n_b = 2.6477$ ($Bi_4Ti_3O_{12}$) [32], with a thickness of $d_{Bi_4Ti_3O_{12}}$ which acts as the material with a higher refractive index ($n_H$) in the Fibonacci structure. On the other hand, the refractive index of graphene varies according to its chemical potential (its conductivity) which the relationship is defined as follows [33]:

$$n_g(\omega) = \sqrt{\frac{1 + \sigma_g}{i\omega\varepsilon_0}} \tag{9}$$

**Table 1** Conclusion information from Fig. 2

| Chemical potential (eV) | Au thickness (nm) | Minimum reflectivity | Sensitivity (deg/RIU) | FWHM (deg) | FoM (1/RIU) |
|---|---|---|---|---|---|
| 0.3 | 40 | 0.007 | 204.20 | 6.66 | 396.68 |
| | 50 | 0.007 | 204.20 | 6.67 | 429.48 |
| | 60 | 0.006 | 204.20 | 6.67 | 454.52 |
| | 70 | 0.006 | 204.20 | 6.68 | 474.15 |
| 0.5 | 40 | 0.070 | 192.19 | 4.39 | 618.66 |
| | 50 | 0.072 | 192.19 | 4.39 | 607.02 |
| | 60 | 0.072 | 186.18 | 4.39 | 580.23 |
| | 70 | 0.073 | 192.19 | 4.40 | 593.55 |
| 0.7 | 40 | 0.317 | 186.18 | 3.48 | 168.30 |
| | 50 | 0.318 | 186.18 | 3.48 | 167.35 |
| | 60 | 0.320 | 186.18 | 3.48 | 166.68 |
| | 70 | 0.321 | 186.18 | 3.48 | 166.19 |
| 0.9 | 40 | 0.570 | 186.18 | 3.20 | 100.66 |
| | 50 | 0.570 | 186.18 | 3.20 | 100.41 |
| | 60 | 0.570 | 186.18 | 3.21 | 100.23 |
| | 70 | 0.570 | 186.18 | 3.21 | 100.11 |

Also, the isotropic surface conductivity $\sigma_g$ of graphene can be expressed as follows [34]:

$$\sigma_g = \frac{ie^2\mu_c}{\pi\hbar^2(\omega + i\tau^{-1})} \tag{10}$$

where $\hbar$ is the reduced Planck constant, $e$ is the electron charge, $\mu_c$ is the chemical potential of graphene, and $\tau$ is the relaxation time of charge carriers. The value of this refractive index is always less than the refractive index of bismuth titanate (even with the change in chemical potential). Therefore, it appears as a material with a lower refractive index ($n_L$) in the Fibonacci structure.

The thickness of graphene thin film is defined as $d_g$ that was selected according to the number of graphene layers ($L$): $d_g = L \times 0.34(nm)$. The glass prism in the proposed sensor is selected SF10 and its refractive index is dependent on the source wavelength and is given as follows [35]:

$$n(\lambda) = \left(\frac{1.62153902\lambda^2}{\lambda^2 - 0.0122241457} + \frac{0.256287842\lambda^2}{\lambda^2 - 0.0595736775} + \frac{1.64447552\lambda^2}{\lambda^2 - 147.468793} + 1\right)^{\frac{1}{2}} \tag{11}$$

The refractive index of thiol-tethered DNA has also been determined 1.35 according to the experimental results at a wavelength of 632.8 nm [36]. The resonance angle of the SPR curve changes with the sample attachment [37]. The effect of the graphene, $Bi_4Ti_3O_{12}$, metal nanolayer thicknesses, and also graphene chemical potential on the SPR curve and performance parameters of the sensor was analyzed and compared with other novel structures.

The graphene chemical potential is one of the most critical factors directly related to the graphene refractive index and thus reflectance coefficient. Figure 2a–d shows the reflectance variation with the incident angle curve at different values $\mu_c$. To study the changes in chemical potential, the number of graphene layers and the thickness of bismuth

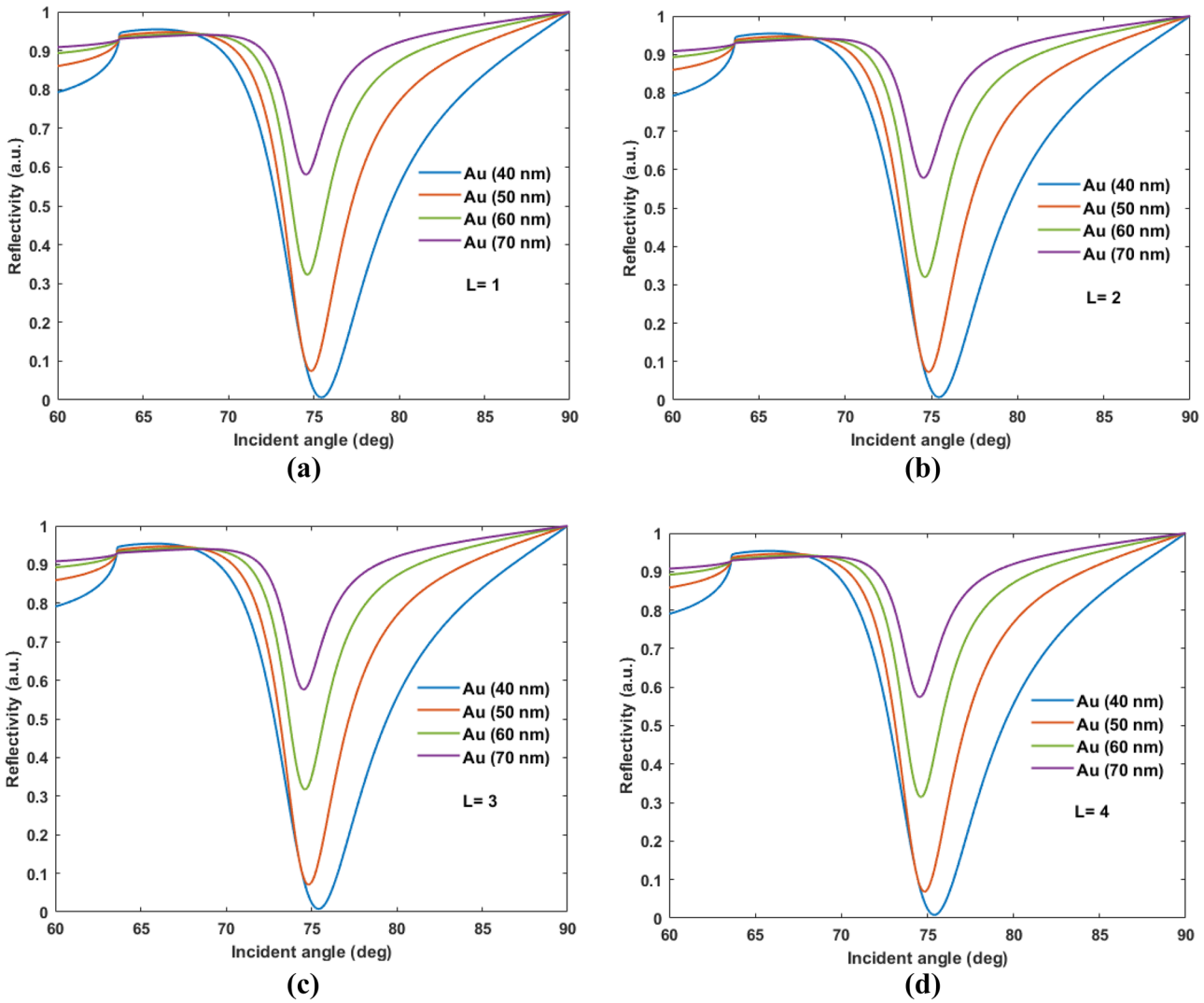


**Fig. 3** The reflectivity in the SPR curve as a function of the number of graphene layers ($L$) with various thicknesses of the gold thin film **a** $L = 1$, **b** $L = 2$, **c** $L = 3$, and **d** $L = 4$; with $\mu_c = 0.3\ eV$ and $d_{Bi_4Ti_3O_{12}} = 19.5\ nm$

titanate were considered fixed, and the thickness of gold thin film also varied from 40 to 70 nm.

As shown in Fig. 2a–d, it is found that the resonance angle remains almost constant, and reflectance minima also increase from 0.006 to 0.570 (a.u.) as the chemical potential changes from 0.3 to 0.9 eV. Therefore, increasing the chemical potential can increase the reflectance and decrease absorption. Table 1 provides concluding information in Fig. 2.

The increasing chemical potential of graphene leads to a decrease in the sensitivity of the proposed structure. In addition, FWHM decreases from 6.68 to 3.20 (deg), which increases the sensor resolution. The best value for the FoM parameter is 618.66 (1/RIU), obtained at a chemical potential of 0.5 eV and a thickness of a 40-nm gold thin film.

To optimize the number of graphene layers, the changes of minimum reflectivity are plotted with various thicknesses of the gold thin film (i.e., 40 nm, 50 nm, 60 nm, 70 nm) at a constant thickness of bismuth titanate. Figure 3a–d shows the reflectance versus incident angle curve for the number of different graphene layers in the proposed configuration. When the number of graphene layers is fixed, the resonance angle shifts to smaller angles as the gold thickness increases. The lowest reflection is obtained for single-layer graphene at a gold thickness of 40 nm. As shown in SPR curves in Fig. 3a–d, the reflectance minima decrease, and therefore, the absorption increases with an increasing number of graphene layers.

The performance parameters of the sensor for the number of graphene layers are listed in Table 2. As shown in Table 2, with the increasing number of graphene layers, the minimum reflectivity has occurred in larger quantities, and FWHM is also reduced. As the number of graphene layers increases to $L = 3$, the sensitivity first decreases and then remains constant. It seems that the few-layer graphene has a high energy barrier and high absorption efficiency. In an SPR sensor, the resolution depends on the FWHM of the reflectivity curve. The high resolution and sensing accuracy are the results of lower FWHM. As can be seen in Table 2, with the increasing number of graphene layers, the FWHM parameter has decreased from 6.67 (deg) (for $L = 1$) to 3.20 (deg) (for $L = 4$).

Similarly, the reflectance curve was plotted for different thicknesses of $Bi_4Ti_3O_{12}$. The resonance angles are shifted to higher angles as the $Bi_4Ti_3O_{12}$ thickness has increased from 6.5 to 26 nm and reflectance minima increase from 0.008 to 0.585 (a.u.) as shown in Fig. 4a–d.

The $Bi_4Ti_3O_{12}$ thickness analysis showed that for the thickness of 6.5 nm in this configuration, the sensitivity would be 258.25 (deg/RIU). A comparison between the performance parameters of the sensor with different thicknesses of $Bi_4Ti_3O_{12}$ is listed in Table 3. As Table 3 shows, at a constant thickness of bismuth titanate, the sensitivity has been dramatically improved with the increasing thickness of the gold thin film, but the FWHM has also increased, which is undesirable. In addition, the results show that the sensitivity in this configuration is more affected by the gold thickness changes while the changes of sensitivity were less than the changes in gold thickness (in the case of investigation of the chemical potential of graphene and the number of graphene layers). From the comparison between the results of graphene layer thickness changes and changes in $Bi_4Ti_3O_{12}$ layer thickness, it can be seen that the performance of the sensor strongly depends on the geometry of the structure because the number of layers with a lower refractive index in the Fibonacci structure is less than the number of layers with the higher refractive index.

**Table 2** Conclusion information from Fig. 3

| Number of graphene layers | Au thickness (nm) | Minimum reflectivity | Sensitivity (deg/RIU) | FWHM (deg) | FoM (1/RIU) |
|---|---|---|---|---|---|
| $L = 1$ | 40 | 0.006 | 198.19 | 6.64 | 476.16 |
| | 50 | 0.006 | 204.20 | 6.65 | 441.28 |
| | 60 | 0.007 | 204.20 | 6.66 | 396.68 |
| | 70 | 0.008 | 204.20 | 6.67 | 359.83 |
| $L = 2$ | 40 | 0.074 | 192.19 | 4.38 | 588.27 |
| | 50 | 0.072 | 192.19 | 4.38 | 603.20 |
| | 60 | 0.070 | 192.19 | 4.39 | 618.66 |
| | 70 | 0.068 | 192.19 | 4.39 | 634.68 |
| $L = 3$ | 40 | 0.322 | 186.18 | 3.48 | 165.75 |
| | 50 | 0.320 | 186.18 | 3.48 | 167.02 |
| | 60 | 0.317 | 186.18 | 3.48 | 168.30 |
| | 70 | 0.314 | 186.18 | 3.48 | 169.61 |
| $L = 4$ | 40 | 0.580 | 186.18 | 3.20 | 100.01 |
| | 50 | 0.578 | 186.18 | 3.20 | 100.33 |
| | 60 | 0.576 | 186.18 | 3.20 | 100.66 |
| | 70 | 0.574 | 186.18 | 3.21 | 100.99 |

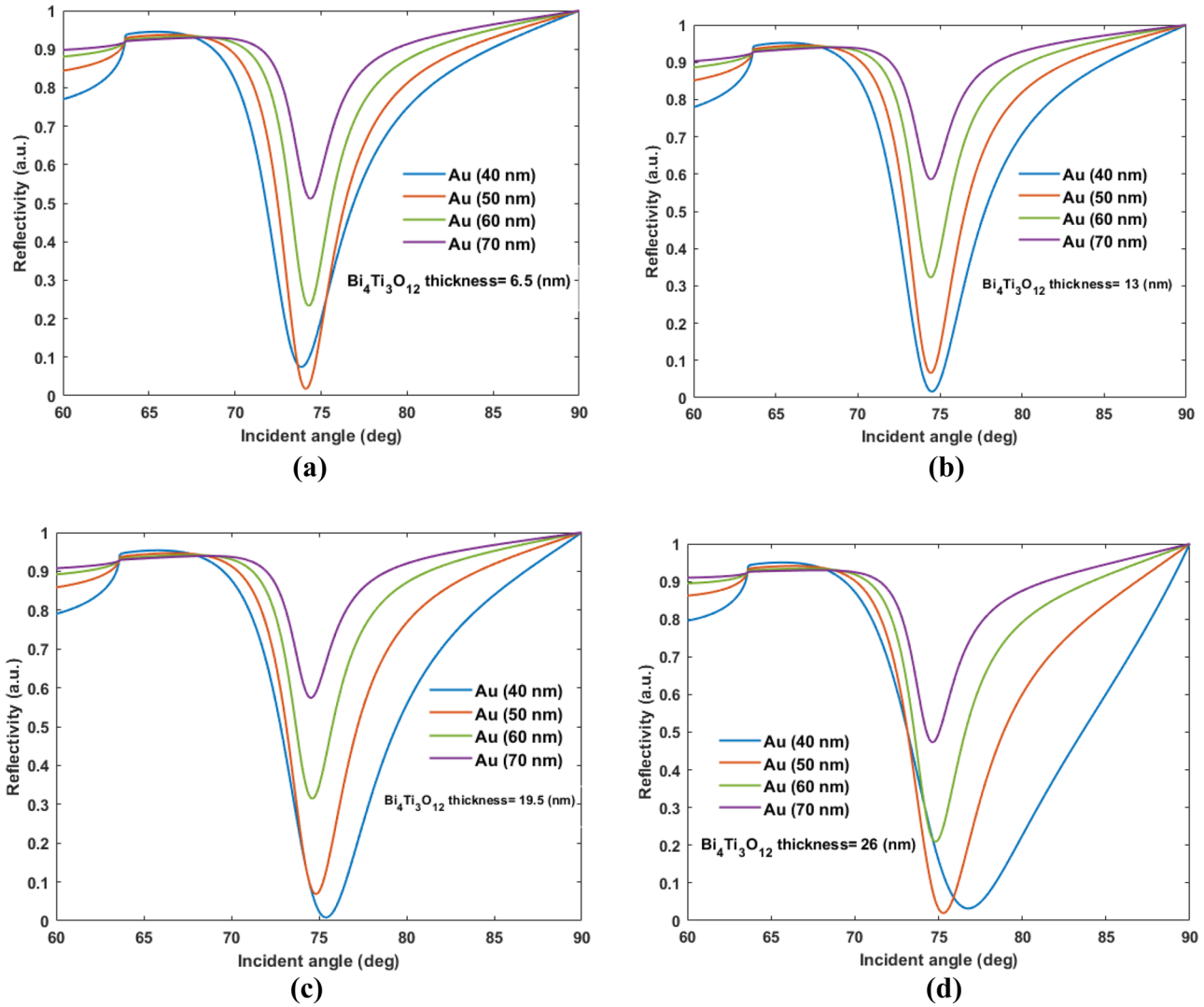


**Fig. 4** The reflectivity in the SPR curve as a function of the $Bi_4Ti_3O_{12}$ thicknesses with various thicknesses of the gold thin film **a** $Bi_4Ti_3O_{12}$ thicknesses = 6.5 nm, **b** $Bi_4Ti_3O_{12}$ thicknesses = 13 nm, **c** $Bi_4Ti_3O_{12}$ thicknesses = 19.5 nm, and **d** $Bi_4Ti_3O_{12}$ thicknesses = 26 nm; with values of $\mu_c = 0.3\ eV$ and $d_g = 4 \times 0.34\ nm$

The thickness of the layers was optimized in a layer-wise procedure to achieve maximum sensor performance. Initially, the effect of the thickness of each layer on the reflectivity as a function of incident angle and sensitivity was investigated and the thickness of the other layers was kept constant. After optimizing the thickness of each layer, this process was repeated for the other layers. The goal was to get the lowest $R_{\min}$ (minimum value of the reflectivity curve) at the same time the most sensitivity. This process was performed for gold, graphene, and bismuth titanate layers. Figure 5 shows the 3D diagrams depicting the sensitivity as a function of the chemical potential of graphene, the number of graphene layers, and bismuth titanate thickness simultaneously. From Fig. 5a, the highest sensitivity value seemed attainable with lower thicknesses of bismuth titanate and a large number of graphene layers.

According to the above results, the optimal thickness of the gold thin film was considered 50 nm. Although the sensitivity can increase in a specific range according to the results, increasing sensitivity can be accompanied by a decrease in the FoM parameter. Therefore, a compromise will be made to obtain the optimal value of sensitivity and the FoM parameter simultaneously. To meet this demand, the optimum thickness for bismuth titanate and the number of graphene layers should be 19.5 nm and $L = 4$, respectively. Figure 5b also shows the sensitivity changes for the chemical potential of graphene (graphene refractive index) at different thicknesses of graphene. It is clear that the

**Table 3** Conclusion information from Fig. 4

| $Bi_4Ti_3O_{12}$ thickness (nm) | Au thickness (nm) | Minimum reflectivity | Sensitivity (deg/RIU) | FWHM (deg) | FoM (1/RIU) |
|---|---|---|---|---|---|
| 6.5 | 40 | 0.074 | 162.16 | 5.54 | 392.18 |
| | 50 | 0.016 | 180.18 | 5.51 | 198.66 |
| | 60 | 0.008 | 204.20 | 6.67 | 359.83 |
| | 70 | 0.032 | 258.25 | 10.73 | 744.09 |
| 13 | 40 | 0.017 | 174.17 | 3.98 | 247.94 |
| | 50 | 0.066 | 180.18 | 3.93 | 691.02 |
| | 60 | 0.068 | 192.19 | 4.39 | 634.68 |
| | 70 | 0.019 | 210.21 | 5.85 | 179.63 |
| 19.5 | 40 | 0.023 | 174.17 | 3.30 | 225.64 |
| | 50 | 0.322 | 180.18 | 3.27 | 170.82 |
| | 60 | 0.314 | 186.18 | 3.48 | 169.61 |
| | 70 | 0.020 | 192.19 | 4.11 | 223.04 |
| 26 | 40 | 0.511 | 180.18 | 3.12 | 112.80 |
| | 50 | 0.585 | 186.18 | 3.09 | 102.81 |
| | 60 | 0.574 | 186.18 | 3.21 | 100.99 |
| | 70 | 0.473 | 186.18 | 3.55 | 110.59 |

sensitivity at $L = 2$ suddenly decreases for all chemical potential values. The high real part refractive index of graphene layers and the high dielectric constant of $Bi_4Ti_3O_{12}$ can enhance the evanescent field at the metal interface and serve the absorption medium. In the Fibonacci structure, the refractive index effect of the bismuth titanate layer can be more effective because, in this structure, the number of layers with a higher refractive index (bismuth titanate) is more than the number of layers with a lower refractive index (graphene).

Figure 6 shows the reflectance curves for analyte refractive index changes from 1.33 to 1.35 in steps of 0.005. Any change in the refractive index of the sensing medium causes a change in the resonance angle of the surface plasmon, and consequently the sensor sensitivity changes. After the discussions described above, the configuration of SF10 prism-gold thin film-Fibonacci structure-thiol-tethered DNA-sensing medium was optimized and the reflection curve is plotted. The number of graphene layers and $Bi_4Ti_3O_{12}$ thickness determined $L = 4$ and 19.5 nm, respectively. In addition, the optimal refractive index of graphene was calculated by chemical potential and found as a material with a lower refractive index in the Fibonacci structure. In Fig. 6, the reflectance minima of the sensors are reduced with the

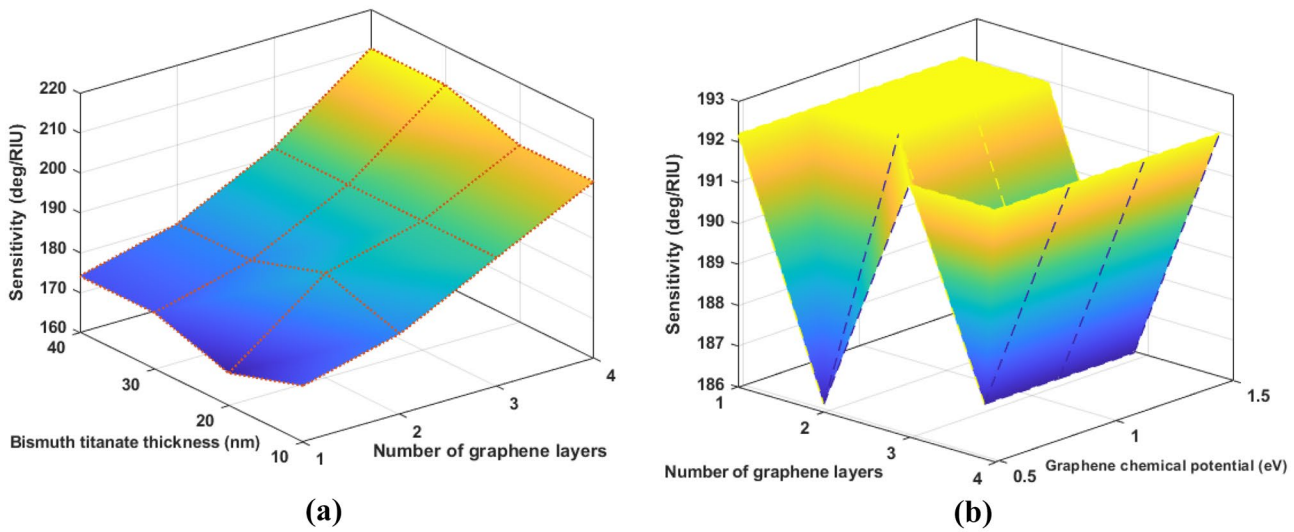


**Fig. 5** The variation of the sensitivity as a function of the chemical potential of graphene, number of graphene layers, and bismuth titanate thickness with 50 nm gold thin film (**a**) The effect of graphene and bismuth titanate thickness changes on sensitivity; (**b**) The effect of graphene chemical potential and bismuth titanate thickness changes on sensitivity

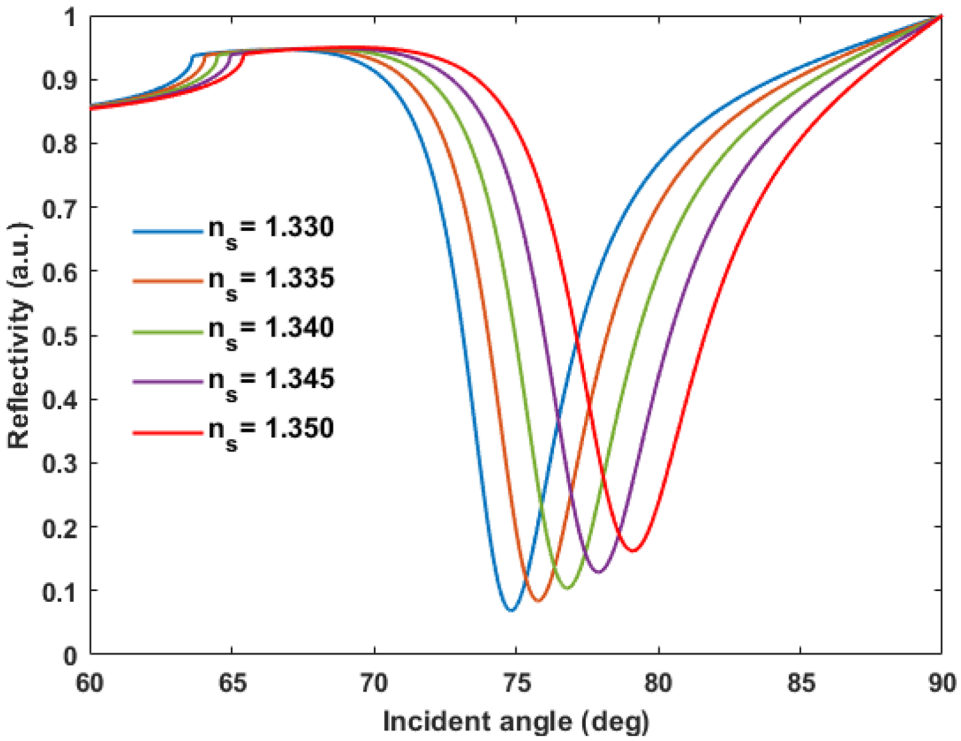


**Fig. 6** Variation of reflectivity in terms of the incident angle of light for analyte coronavirus (as sensing medium) ranging from 1.33 to 1.35 with an interval of 0.005 for SPR sensor with the configuration of SF10 prism-gold layer-Fibonacci structure-thiol tethered DNA-sensing medium

increment of the sensing medium refractive index while the SPR curve is shifting from the left to the right direction.

As Fig. 6 shows, the resonance angles of the SPR curves for SF10/Au (50 nm)/Fibonacci structure (including graphene and $Bi_4Ti_3O_{12}$ layers) are obtained at 74.83°, 75.79°, 76.78°, 77.89°, and 79.09° for analyte coronavirus of 1.330, 1.335, 1.340, 1.345, and 1.350, respectively. With a slight increase in refractive index, there is a noticeable variation in sensitivity as high as 264.26 (deg/RIU) related to the refractive index of 1.350.

Finally, the performance parameters of the proposed configuration with other structures in the field of detection are compared. The sensitivity, FWHM, and FoM were taken into account for comparison. However, sensitivity is the most crucial performance parameter under consideration; FWHM and FoM are also vital for sensing accuracy. The findings of this comparison are presented in Table 4. The proposed design shows higher sensitivity than other structures. The proposed structure simultaneously demonstrated high sensitivity and lower FWHM while some designs have relatively good sensitivity but suffer from higher FWHM.

To reach the intended degree of performance, the sensor arrangement must be correct, as well as the materials employed. Although waveguide-based surface plasmon resonance has a high sensitivity [42], it faces several obstacles. Some of the obstacles that can pose problems in constructing these biosensors are the operating wavelength, proper substrate material selection, and creating sensor surfaces (picking up exact metal) for phase matching. Furthermore, arrangements in which the terminal layer is in direct touch with the sensing medium [40, 41] might generate problems and measurement mistakes. Not only are biomolecules not confined well in this direct contact, but they can also cause a chemical interaction between the detecting medium and the final layer. Silver (Ag) is another metal that is employed in

**Table 4** Sensing performance comparison with other structures

| Sensor configuration | Sensitivity (deg/RIU) | FWHM (deg) | FoM ($RIU^{-1}$) |
|---|---|---|---|
| **This work (proposed structure)** | **192.19** | **4.39** | **634.68** |
| Ag-Si-$BaTiO_3$ [38] | 130.30 | 11.86 | 692.28 |
| Gold nanosheet is functionalized with SARS-CoV-2 spike (S) protein antibody [39] | 111.11 | Not reported | Not reported |
| Mirrored bilayer of Au-$MoS_2$-Graphene [40] | 75.2 | 17 | 44.23 |
| $TiO_2$−$SiO_2$-Ag-$MoS_2$-Graphene [41] | 98 | Not reported | Not reported |
| Au-Graphene [42] | 53.71 | 5 | 85.79 |

biosensor configurations [38, 41]. Unlike gold (Au), it is not inert, and the ion migration phenomena have been observed in this metal, resulting in unfavorable chemical interactions. The suggested biosensor, which uses a prism-based structure and quasi-photonic crystals as well as receptors to trap DNA and biomolecules, is expected to have great sensitivity in practical applications and remove issues like phase mismatching and undesired chemicals.

## Conclusion

In this paper, we provide a sensitivity and accuracy SPR sensor based on a novel configuration for detecting and studying DNA hybridization. A Fibonacci structure made of nanostructured thin films and graphene as a 2D material with localized surface plasmon properties was found to be the best configuration for this sensor. The influence of nanofilm thickness on sensor performance, such as the number of graphene layers and $Bi_4Ti_3O_{12}$ thickness, was investigated. The sensitivity value of 192.19 (deg/RIU) was obtained from this analysis. Because of its excellent sensing capability, the suggested design can be employed in a wide range of high-sensitivity applications, including biomedical applications that detect low quantities of DNA and RNA-based viruses and prevent the occurrence of infectious diseases spread.

**Author Contribution** We confirm that the manuscript has been read and approved by all named authors and that there are no other persons who satisfied the criteria for authorship but are not listed. We further confirm that the order of authors listed in the manuscript has been approved by all of us.

**Availability of Data and Materials** The data that support the findings of this study are available from the corresponding author upon reasonable request.

## Declarations

**Ethics Approval and Consent to Participate** Not applicable.

**Consent to Publication** Not applicable.

**Competing Interests** The authors declare no competing interests.

## References


1. Kim J, Campbell AS, de Ávila BEF, Wang J (2019) Wearable biosensors for healthcare monitoring. Nat Biotechnol 37:389–406
2. Kamal Eddin FB, Fen YW (2020) The principle of nanomaterials based surface plasmon resonance biosensors and its potential for dopamine detection. Molecules 25:2769
3. Pitruzzello G, Krauss TF (2018) Photonic crystal resonances for sensing and imaging. J Opt 20:073004
4. Sabu C, Henna TK, Raphey VR, Nivitha KP, Pramod K (2019) Advanced biosensors for glucose and insulin. Biosens Bioelectron 141:111201
5. Schneider T, Jahr N, Jatschka J, Csaki A, Stranik O, Fritzsche W (2013) Localized surface plasmon resonance (LSPR) study of DNA hybridization at single nanoparticle transducers. J Nanopart Res 15:1–10
6. Patel SK, Parmar J, Kosta YP, Ladumor M, Zakaria R, Nguyen TK, Dhasarathan V (2020) Design of graphene metasurface based sensitive infrared biosensor. Sensors Actuators A Phys 301:111767
7. Kumar A, Yadav AK, Kushwaha AS, Srivastava SK (2020) A comparative study among WS2, MoS2 and graphene based surface plasmon resonance (SPR) sensor. Sensors Actuators Rep 2:00015
8. Müller CM, Pejcic B, Esteban L, Piane CD, Raven M, Mizaikoff B (2014) Infrared attenuated total reflectance spectroscopy: an innovative strategy for analyzing mineral components in energy relevant systems. Sci Rep 1:11
9. Ferreira, ICC, Aguiar EMG, Silva ATF, Santos LLD, Cardoso-Sousa L, Araújo TG, Santos DW, Goulart LR, Sabino-Silva R, Maia YCP (2020) Attenuated total reflection-fourier transform infrared (ATR-FTIR) spectroscopy analysis of saliva for breast cancer diagnosis. J Oncol
10. Shibayama J, Mitsutake K, Yamauchi J, Nakano H (2021) Kretschmann-and Otto-type surface plasmon resonance waveguide sensors in the terahertz regime. Microw Opt Techn Let 63:103–106
11. Taniselass S, Arshad MM, Gopinath SC (2019) Graphene-based electrochemical biosensors for monitoring noncommunicable disease biomarkers. Biosens Bioelectron 130:276–292
12. An G, Li S, Wang H, Zhang X, Yan X (2018) Quasi-D-shaped optical fiber plasmonic refractive index sensor. J Opt 20:035403
13. Iqbal T, Afsheen S (2017) One dimensional plasmonic grating: high sensitive biosensor. Plasmonics 1:19–25
14. Iqbal T, Afsheen S (2016) Coupling efficiency of surface plasmon polaritons for 1D plasmonic gratings: role of under-and over-milling. Plasmonics 5:1247–1256
15. Afsheen S, Munir M, Khan MI, Iqbal T, Abrar M, Tahir MB, Rehman J-U, Riaz KN, Ijaz M, Nabi G (2018) Efficient biosensing through 1D silver nanostructured devices using plasmonic effect. Nanotechnology 38:385501
16. Xie T, He Y, Yang Y, Zhang H, Xu Y (2021) Highly sensitive surface plasmon resonance sensor based on graphene-coated U-shaped fiber. Plasmonics 16:205–213
17. Ghayoor R, Keshavarz A (2019) Design of tunable devices at terahertz frequencies based on quasi-photonic crystals incorporated with graphene. Commun Theor Phys 71:1227
18. Jiang W, Gu L, Chen X, Chen RT (2007) Photonic crystal waveguide modulators for silicon photonics: device physics and some recent progress. Solid State Electron 51:1278–1286
19. Bendjelloul R, Bouchemat T, Bouchemat M, Benmerkhi A (2016) New design of T-shaped channel drop filter based on photonic crystal ring resonator. J Nanosci Nanotechnol 6:13–17
20. Hassan AKS, Mohamed AS, Maghrabi MM, Rafat NH (2015) Optimal design of one-dimensional photonic crystal filters using minimax optimization approach. Appl Opt 54:1399–1409
21. Lu Y, Liu H, Sun Q, Huang N, Wang Z (2016) Terahertz narrow-band filter based on rectangle photonic crystal. J Mod Opt 63:224–230
22. Pacholski C (2013) Photonic crystal sensors based on porous silicon. Sensors 13:4694–4713
23. Bian LA, Liu P, Li G (2016) Design of tunable devices using one-dimensional Fibonacci photonic crystals incorporating graphene at terahertz frequencies. Superlattice Microstruct 98:522–534
24. Phan T (2020) Novel coronavirus: from discovery to clinical diagnostics. Infect Genet Evol 79:104211

25. Nishiura H, Linton NM, Akhmetzhanov AR (2020) Serial interval of novel coronavirus (COVID-19) infections. Int J Infect Dis 93:284–286
26. Jiang S, Xia S, Ying T, Lu L (2020) A novel coronavirus (2019-nCoV) causing pneumonia-associated respiratory syndrome. Cell Mol Immunol 17:554–554
27. Jin X, Lian JS, Hu JH, Gao J, Zheng L, Zhang YM, Yang Y (2020) Epidemiological, clinical and virological characteristics of 74 cases of coronavirus-infected disease 2019 (COVID-19) with gastrointestinal symptoms. Gut 69:1002–1009
28. Lu S, Lin J, Zhang Z, Xiao L, Jiang Z, Chen J, Luo S (2021) Alert for non-respiratory symptoms of coronavirus disease 2019 patients in epidemic period: a case report of familial cluster with three asymptomatic COVID-19 patients. J Med Virol 93:518–521
29. Sahel S, Amri R, Bouaziz L, Gamra D, Lejeune M, Benlahsen M, Bouchriha H (2016) Optical filters using Cantor quasi-periodic one dimensional photonic crystal based on Si/SiO2. Superlattice Microstruct 97:429–438
30. Alagdar M, Yousif B, Areed NF, Elzalabani M (2020) Improved the quality factor and sensitivity of a surface plasmon resonance sensor with transition metal dichalcogenide 2D nanomaterials. J Nanoparticle Res 22:1–13
31. Rahman MM, Rana MM, Rahman MS, Anower MS, Mollah MA, Paul AK (2020) Sensitivity enhancement of SPR biosensors employing heterostructure of PtSe2 and 2D materials. Opt Mater 107:110123
32. Malitson IH (1965) Interspecimen comparison of the refractive index of fused silica. Josa 55:1205–1209
33. Xu J (2018) Linear optical characterization of graphene structure. University of Waterloo (Master's thesis)
34. Dai X, Jiang L, Xiang Y (2015) Tunable THz angular/frequency filters in the modified Kretschmann-Raether configuration with the insertion of single layer graphene. IEEE Photonics J 7:1–8
35. Ouyang Q, Zeng S, Jiang L, Hong L, Xu G, Dinh XQ, Yong KT (2016) Sensitivity enhancement of transition metal dichalcogenides/silicon nanostructure-based surface plasmon resonance biosensor. Sci Rep 6:1–13
36. Peterlinz KA, Georgiadis RM, Herne TM, Tarlov MJ (1997) Observation of hybridization and dehybridization of thiol-tethered DNA using two-color surface plasmon resonance spectroscopy. J Am Chem Soc 119:3401–3402
37. Prevenslik T (2020) Mystery pulmonary and neurological symptoms by EM radiation from the Coronavirus
38. Uddin SMA, Chowdhury SS, Kabir E (2021) Numerical analysis of a highly sensitive surface plasmon resonance sensor for sars-cov-2 detection. Plasmonics 16:2025–2037
39. Das CM, Guo Y, Yang G, Kang L, Xu G, Ho HP, Yong KT (2020) Gold nanorod assisted enhanced plasmonic detection scheme of COVID-19 SARS-CoV-2 spike protein. Adv Theory Simul 3:2000185
40. Chowdhury SS, Uddin SMA, Kabir E (2020) Numerical analysis of sensitivity enhancement of surface plasmon resonance biosensors using a mirrored bilayer structure. Photonics Nanostruct 41:100815
41. Moznuzzaman M, Islam MR, Hossain MB, Mehedi IM (2020) Modeling of highly improved SPR sensor for formalin detection. Results Phys 16:102874
42. Rahman MS, Anower MS, Bashar LB, Rikta KA (2017) Sensitivity analysis of graphene coated surface plasmon resonance biosensors for biosensing applications. Sens Bio-sens Res 16:41–45